ADVANCES IN ATMOSPHERIC SCIENCES, VOL. 35, AUGUST 2018, 1035–1048

• **Original Paper** •

Indian Ocean SST modes and Their Impacts as Simulated in BCC_CSM1.1(m) and HadGEM3

Bo LU[1,2,3], Hong-Li REN*[1,2,4], Rosie EADE[5], and Martin ANDREWS[5]

[1]*Laboratory for Climate Studies, National Climate Center, China Meteorological Administration, Beijing* 100081 *China*
[2]*CMA-NJU Joint Laboratory for Climate Prediction Studies, Institute for Climate and Global Change Research, School of Atmospheric Sciences, Nanjing University, Nanjing* 210023*, China*
[3]*Xin Jiang Climate Center, Ürümqi* 830002*, China*
[4]*Department of Atmospheric Science, School of Environmental Studies, China University of Geoscience, Wuhan* 430074*, China*
[5]*Met Office Hadley Center, Exeter* EX1 3PB*, UK*

(Received 6 November 2017; revised 24 February 2018; accepted 4 March 2018)

ABSTRACT

The sea surface temperature anomalies (SSTAs) in the tropical Indian Ocean (TIO) show two dominant modes at interannual time scales, referred to as the Indian Ocean basin mode (IOBM) and dipole mode (IOD). Recent studies have shown that the IOBM and IOD not only affect the local climate, but also induce remarkable influences in East Asia via teleconnections. In this study, we assess simulations of the IOBM and IOD, as well as their teleconnections, using the operational seasonal prediction models from the Met Office (HadGEM3) and Beijing Climate Center [BCC_CSM1.1(m)]. It is demonstrated that the spatial patterns and seasonal cycles are generally reproduced by the control simulations of BCC_CSM1.1(m) and HadGEM3, although spectra biases exist. The relationship between the TIO SSTA and El Niño is successfully simulated by both models, including the persistent IOBM warming following El Niño and the IOD–El Niño interactions. BCC_CSM1.1(m) and HadGEM3 are capable of simulating the observed local impact of the IOBM, such as the strengthening of the South Asian high. The influences of the IOBM on Yangtze River rainfall are also captured well by both models, although this teleconnection is slightly weaker in BCC_CSM1.1(m) due to the underestimation of the northwestern Pacific subtropical high. The local effect of the IOD on East African rainfall is reproduced by both models. However, the remote control of the IOD on rainfall over southwestern China is not clear in either model. It is shown that the realistic simulations of TIO SST modes and their teleconnections give rise to the source of skillful seasonal predictions over China.

Key words: Indian Ocean SST, teleconnection, simulation, seasonal prediction

Citation: Lu, B., H.-L. Ren, R. Eade, and M. Andrews, 2018: Indian Ocean SST modes and their impacts as simulated in BCC_CSM1.1(m) and HadGEM3. *Adv. Atmos. Sci.*, **35**(8), 1035–1048, https://doi.org/10.1007/s00376-018-7279-3.

1. Introduction

Sea surface temperature anomalies (SSTAs) in the tropical Indian Ocean (TIO) exhibit two dominant modes on interannual time scales. The first empirical orthogonal function (EOF) mode shows a uniform SSTA over the entire TIO basin, which is referred to as the Indian Ocean basin mode (IOBM). The second EOF mode—namely, the Indian Ocean dipole mode (IOD)—exhibits a cooling (warming) off the Sumatran coast and a warming (cooling) over the western equatorial Indian Ocean. The IOBM accounts for about 39% of the total variance of the TIO SSTA, while the IOD explains about 11%.

The IOBM is believed to be controlled by the El Niño–Southern Oscillation (ENSO) (Wallace et al., 1998). During El Niño, atmospheric convection is suppressed over the Indian Ocean, and the resultant increase in solar radiation contributes to the basin-wide warming over the TIO (Chiang and Sobel, 2002). Forced by the heat flux changes, the warming of the TIO often occurs during El Niño development and persists after the mature phase of El Niño events (Klein et al., 1999; Liu and Alexander, 2007). This basin-wide warming plays an important role in modulating the local and remote climate. The interannual variability of the South Asian high (SAH) has been found to be forced by the IOBM (Yang et al., 2007; Yang and Liu, 2008). When the TIO warms up, the SAH strengthens and exhibits a southward extension due to the heating in the boundary layer (Huang et al., 2011). The basin-wide warming over the TIO also induces an eastward propagating Kelvin wave, which strengthens the anticyclone over the subtropical northwestern Pacific and then increases

* Corresponding author: Hong-Li REN
Email: renhl@cma.gov.cn

the summer rainfall over the Yangtze River valley (Xie et al., 2009).

The dynamics of IOD events is still unsolved, especially for its relationship with ENSO. A number of studies have argued its dependence on ENSO (Allan et al., 2001; Baquero-Bernal et al., 2002; Dommenget and Latif, 2002; Dommenget and Jansen, 2009). However, other studies point out the importance of the internal air–sea interaction within the Indian Ocean basin (Behera et al., 1999; Webster et al., 1999; Ashok et al., 2003; Yamagata et al., 2003). The IOD not only affects the local rainfall around the Indian Ocean, such as Australia (Ashok et al., 2003) and East Africa (Black et al., 2003), but also influences global climate variability (Saji and Yamagata, 2003) via atmospheric teleconnection with regions, such as East Asia (Yuan et al., 2008; Qiu et al., 2014) and South America (Chan et al., 2008).

Considering the remarkable climatic impacts of Indian Ocean SST modes, they could serve as sources for skillful seasonal predictions if our operational models can reproduce a realistic IOBM and IOD and their teleconnections. In this study, we assess simulations of Indian Ocean SST by two operational seasonal prediction models, from the Beijing Climate Center and the UK Met Office respectively. We also explore how well our models can capture the TIO SST teleconnections and whether the simulations of TIO SST modes can influence the seasonal rainfall predictions over China. The remainder of the paper is organized as follows:

Section 2 describes the observations, control experiment and hindcast datasets used in the study. In section 3 we evaluate the control simulations of the IOBM and IOD in the operational models. Local and remote climate impacts of TIO SST in the models are investigated in section 4, with a comparison to seasonal forecasting systems. Finally, a summary and discussion of the results is given in section 5.

2. Data and methods

2.1. *Observational data*

This study utilizes HadISST (Rayner et al., 2006) for the observed monthly mean SST, CRU TS Version 4.01 (Harris et al., 2014) for the observed grid precipitation over land, and NCEP–DOE Reanalysis-1 (Kalnay et al., 1996) for the horizontal wind and geopotential height. The horizontal grid resolutions of these datasets are $1^\circ \times 1^\circ$, $1^\circ \times 1^\circ$ and $2.5^\circ \times 2.5^\circ$, respectively. For consistency with the period of the Reanalysis-1 data, the common period of 1948–2016 is analyzed for the observation.

2.2. *Operational climate model at the Beijing Climate Center*

Version 1.1 (moderate resolution) of the Beijing Climate Center's Climate System Model, i.e., BCC_CSM1.1(m), is currently employed as the operational model for seasonal prediction at the Beijing Climate Center. The model details are described in Wu et al. (2010). The output from a 400-year pre-industrial control experiment is analyzed to obtain a robust assessment of the Indian Ocean SST modes and their impacts in BCC_CSM1.1(m). A set of seasonal hindcasts, performed at the beginning of every month, with 24 members per prediction, from 1991 to 2014, are also assessed. The hindcast design of BCC_CSM1.1(m) is described in detail in Lu et al. (2017).

2.3. *Operational climate model at the UK Met Office*

Version 5 of the Global Seasonal Forecasting System (GloSea5) is the current operational seasonal forecasting system of the UK Met Office. The HadGEM3 coupled model is used in GloSea5. The model details are introduced by MacLachlan et al. (2015). In an effort to obtain the robust features of Indian Ocean SST and associated teleconnections in HadGEM3, a 100-year pre-industrial control experiment is utilized. Seasonal hindcast experiments of GloSea5 are also assessed; 24 members are performed for boreal summer (winter), initialized on 25 April (October), 1 May (November) and 9 May (November) from 1992 to 2011. The hindcast design of Glosea5 is described by MacLachlan et al. (2015).

3. Simulations of the IOBM and IOD

Figure 1 illustrates the climatological SST and horizontal wind at 850 hPa over the TIO domain. Winds over the northern Indian Ocean reverse direction from northeasterly (Fig. 1a) during boreal winter to southwesterly during boreal summer (Fig. 1d), which exhibits a typical monsoon climate. As a result, the trade wind over the TIO is very weak compared with that over the tropical Pacific, and the annual mean westerly wind is evident. Thus, the upwelling is stronger and the SST is cooler in the western Indian Ocean than in the eastern side.

The seasonal reversal of low-level wind is generally reproduced well by BCC_CSM1.1(m) and HadGEM3, with a realistic northeasterly wind in boreal winter and southwesterly wind in boreal summer. For BCC_CSM1.1(m), the westerly wind between the equator and 10°S in January is slightly stronger than in the observations, and the northwesterly wind off the Sumatran coast is overestimated (Fig. 1b). Thus, the thermocline in the eastern Indian Ocean is deeper in BCC_CSM1.1(m) than that observed (Lu et al., 2017), which implies an underestimation of the air–sea interaction in the eastern TIO. For HadGEM3, the tropical SST is warmer than in the observations (Figs. 1c and f). In January, the observed equatorial westerly wind is missed in HadGEM3 (Fig. 1c), leading to the underestimation of the zonal SST gradient along the equator in boreal winter. In July, the southeastern wind off the Sumatran coast is too strong and an unrealistic cross-equator wind over the eastern TIO is evident in HadGEM3. As a result, the thermocline is shallower (Johnson et al., 2017) than observed and the air–sea interaction in the southeastern TIO is too active in HadGEM3.

We further evaluate the leading modes of the TIO SST in BCC_CSM1.1(m) and HadGEM3 at interannual time scales. EOF analysis is performed on the monthly mean SST in the

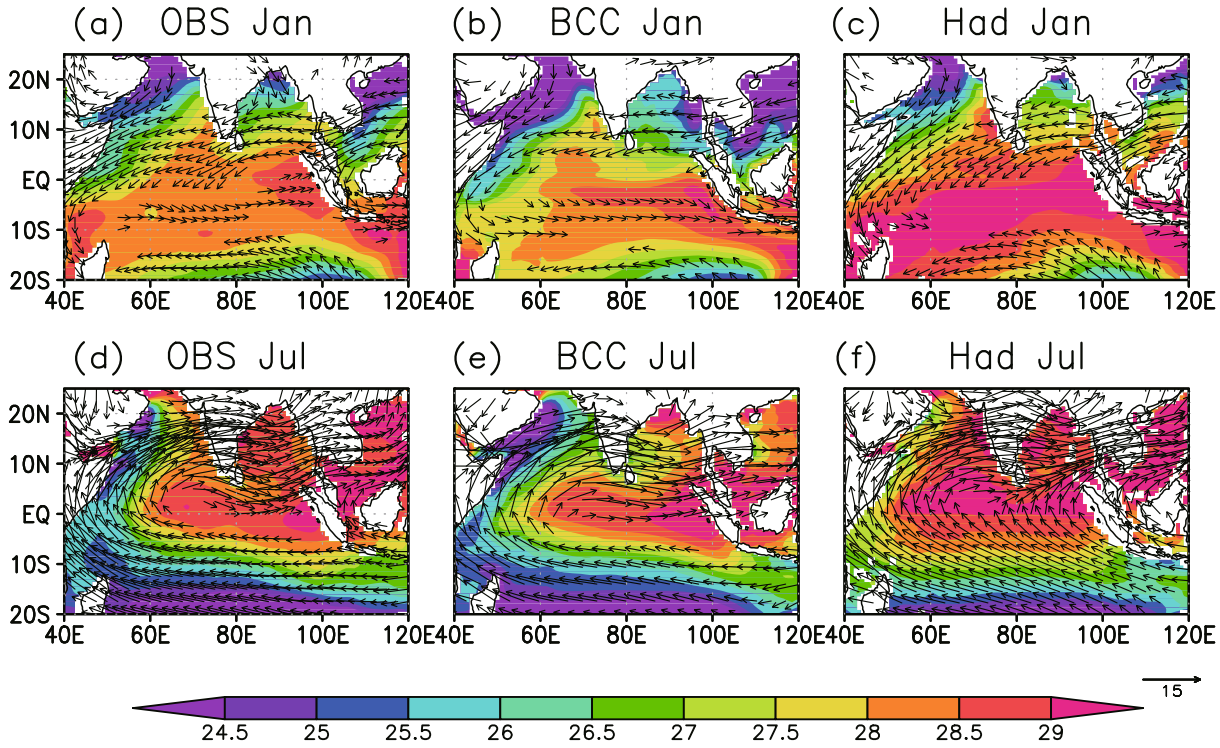

Fig. 1. Climatological patterns of SST (units: °C) and horizontal wind at 850 hPa (units: m s^{-1}) over the TIO during (a–c) January and (d–f) July, in the (a, d) observation and the simulations by (b, e) BCC_CSM1.1(m) and (c, f) HadGEM3 (c, f).

TIO (15°S–30°N, 25°–120°E) for all calendar months. To focus on the interannual variability, the remarkable warming trend in TIO SST (Du and Xie, 2008) has been removed linearly. As shown in Fig. 2, the two leading modes in BCC_CSM1.1(m) and HadGEM3 show similar features to the observations. The first EOF mode shows the basin-wide warming in the observations, which is generally simulated well by both models (Figs. 2b and c). The first EOF mode in BCC_CSM1.1(m) (HadGEM3) explains 25% (24%) of the total variance, which is smaller than that in the observation. Du et al. (2013) investigated the leading EOF modes of TIO SST among CMIP5 models and showed similar results that the explained variance of this basin mode is underestimated by many state-of-the art models that participating in CMIP5. The observed second EOF mode shows a zonal dipole feature, with reverse SST changes between the western and southeastern TIO. Both models generally capture the zonal dipole pattern in the second EOF mode (Figs. 2e and f). The second EOF mode in BCC_CSM1.1(m) (HadGEM3) explains 15% (10%) of the total variance, which is comparable to that in the observation.

Although both models capture the general features of the observed leading modes, some distinct biases still exist. For the first mode, the positive signal in BCC_CSM1.1(m) locates in the western TIO, while a weak negative signal occurs in the eastern basin. As indicated by Du et al. (2013), this bias pattern is also evident in several CMIP5 models, such as ACCESS1.0, HadGEM2-ES, and MPI-ESM-LR. On the other hand, the pronounced positive signal in HadGEM3 is constrained in the central TIO. For the second mode, the negative signal in BCC_CSM1.1(m) locates in the northeastern TIO, while the observed negative signal locates in the southeastern TIO. In addition, the distribution of the negative signal is constrained to the east of 80°E; however, the simulated patterns show a westward extension of the negative signal in both models. Efforts have been made to understand the causes of this cold-tongue-type distribution bias in the simulated EOF2 (IOD).

Previous studies have shown that the wind–evaporation–SST (WES) feedback is crucial to IOD growth (Li et al., 2003; Liu et al., 2011). The cooling over the eastern TIO will induce an easterly wind anomaly, which may then cool the local SST by increasing the evaporation if the climatological wind is also easterly. Figure 3 demonstrates the mean state of the zonal wind at 850 hPa along the TIO during boreal fall, when IOD events often reach their mature phase. In the observation, the easterly trade wind is pronounced in the eastern TIO; however, westerly wind is evident in the central TIO. As a result of the inactive WES feedback in the central TIO, the negative node of the observed IOD mode is constrained in the eastern TIO. In HadGEM3, the climatological easterly wind is pronounced over the entire TIO. Thus, the simulated WES feedback is also active in the central TIO, which gives rise to the cold tongue distribution in the simulated EOF2 in HadGEM3. The climatological zonal wind in BCC_CSM1.1(m) is consistent with the observation overall. However, in the central TIO, an easterly wind bias is also evident, which may extend the eastern node of the

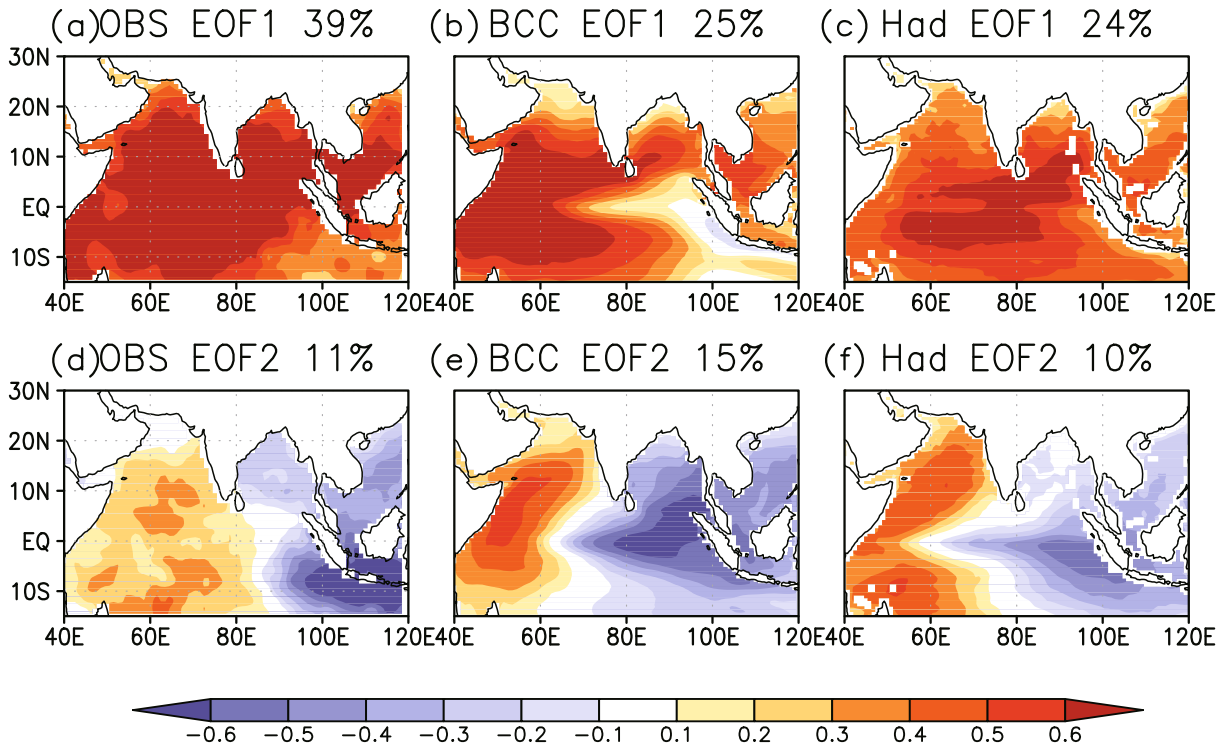

Fig. 2. Spatial patterns of the leading two EOF modes for TIO SST in the (a, d) observations and the simulations by (b, e) BCC_CSM1.1(m) and (c, f) HadGEM3. The explained variances are indicated.

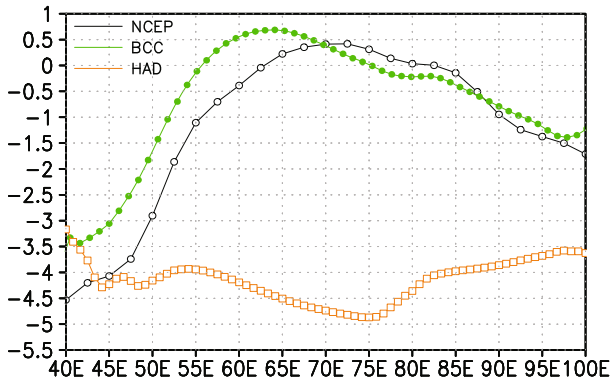

Fig. 3. Climatological zonal wind at 850 hPa averaged over the TIO (10°S–10°N) during November in NCEP Reanalysis-1 (black), BCC_CSM1.1(m) (green), and HadGEM3 (orange).

simulated IOD in BCC_CSM1.1(m). It should be noted that the mean state biases in zonal wind might also affect the ocean-current advection. Due to the lack of availability of three-dimensional ocean data, this effect is not discussed here.

This strong easterly wind bias in the TIO as shown above is a common problem for most CMIP5 models (Li et al., 2015). Their analyses show that such bias can be traced back to errors in the South Asian summer monsoon (SASM). The simulated SASM is generally too weak in most models, which leads to weakened cross-equatorial low-level wind over the western basin and further generates a warm SST bias over the western equatorial Indian Ocean. This warm bias over the western equatorial Indian Ocean is prolonged to the boreal autumn, when Bjerknes feedback helps amplify the error into the equatorial easterly bias over the TIO. Following the above argument by Li et al. (2015), we further explore the causes of the equatorial easterly bias in HadGEM3. The simulated summer [June–July–August (JJA)] rainfall over South Asia (10°–25°N, 70°–90°E) is 4.3 mm d^{-1}, which is much weaker than the observed rainfall of 8.8 mm d^{-1}. As a result of the underestimation of the SASM, the climatological SST over the western TIO (10°S–10°N, 40°–60°E) is remarkably warmer in HadGEM3 (28.1°C) than in the observation (26.4°C) during boreal summer (JJA). This warm bias is prolonged to boreal autumn [September–October–November (SON)], with the mean SST over the western TIO staying 0.7°C warmer than in the observation. Thus, the equatorial easterly bias in HadGEM3 is generated by this warm SST bias over western TIO when Bjerknes feedback becomes active during boreal autumn (Li et al., 2015).

Figure 4 illustrates the seasonal cycle of the principle component (PC) for the two leading modes. The basin-wide warming mode is strong in boreal winter and spring but weak in boreal summer and fall, which is simulated well by both BCC_CSM1.1(m) and HadGEM3 (Fig. 4a). The dipole mode is active during boreal summer and fall in the observation (Fig. 4b), when the mean upwelling becomes strong and the mean thermocline is shallow in the eastern TIO [e.g., as reviewed by Schott et al. (2009)]. HadGEM3 reproduces the observed seasonal cycle of the dipole mode. However,

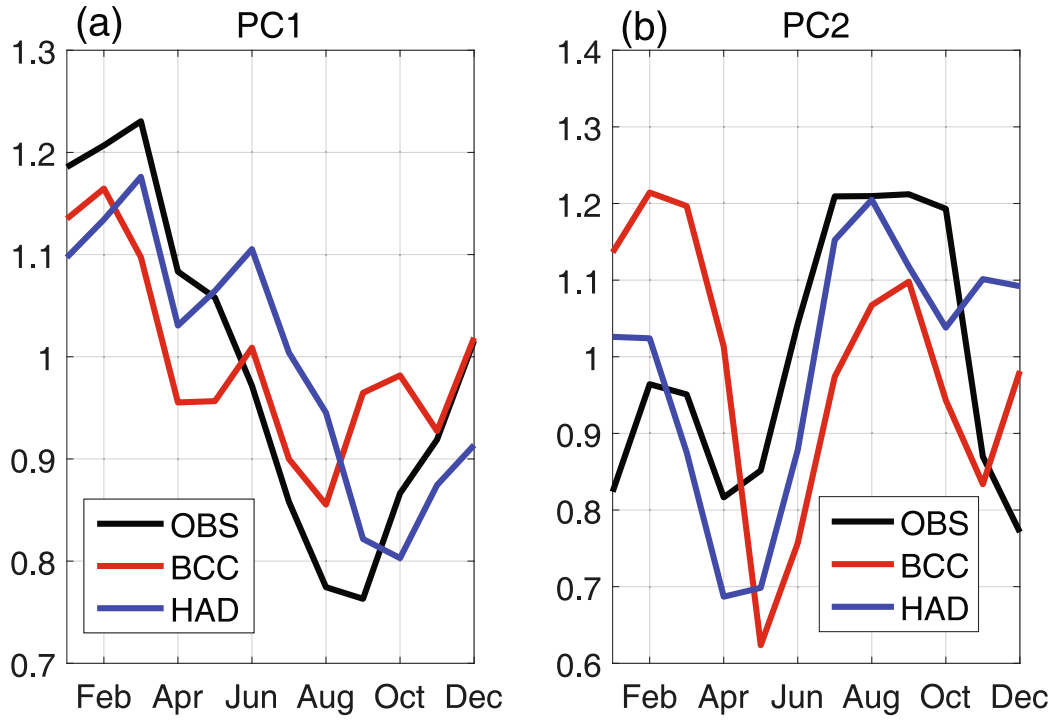

Fig. 4. Seasonal cycles of the standard deviation of (a) EOF PC1 and (b) EOF PC2 in the observation (black) and the simulations by BCC_CSM1.1(m) (red) and HadGEM3 (blue).

BCC_CSM1.1(m) overestimates its amplitude in late winter and early spring. We further investigate their periodicity features by applying wavelet analysis (Fig. 5). To ensure statistical robustness for the computation of spectra (Wittenberg, 2009; Stevenson et al., 2010), simulations with long lengths are necessary. As a result, the wavelet analysis is performed upon the whole period for the model simulations. The spectrum of the first PC peaks from three years to five years, which is consistent with the periodicity of ENSO. However, BCC_CSM1.1(m) tends to simulate a quasi-two-year period for the IOBM, which is much shorter than in the observation (Fig. 5g). The reason for this periodicity bias is related to the simulation of ENSO in BCC_CSM1.1(m). Due to the underestimated air–sea interaction over the tropical Pacific, the period of ENSO in BCC_CSM1.1(m) is about two years (Lu and Ren, 2016a). As a result of the dominant control of ENSO forcing on the IOBM, the short period bias is also evident here. On the contrary, HadGEM3 has a peak spectrum at seven years, which is longer than in the observation. For the IOD spectrum, a sharp peak of five years is observed (Fig. 5h). However, the simulated IOD spectrum is relatively too broad in both models. Overall, both BCC_CSM1.1(m) and HadGEM3 are able to simulate the observed IOBM and IOD as their two leading modes. The spatial patterns and seasonal cycles are generally captured well by both models, although biases in the spectra are evident.

We adopt an IOBM index definition as the average of the SSTAs over (20°S–20°N, 40°–110°E). We also follow the definition of the IOD index given by Saji et al. (1999) by taking the SSTA difference between the western (10°S–10°N, 60°–80°E) and eastern (10°S–0°, 90°–110°E) Indian Ocean regions. As shown in Table 1, these two indices are very good representations of the two leading modes. Hereafter, these simplified indices are used to indicate the IOBM and IOD events in the observations and model simulations.

Table 1. Correlation coefficients between the IOBM (IOD) indices and the PC of the first (second) EOF mode in the observation and the simulations by BCC_CSM1.1(m) and HadGEM3.

	OBS	BCC_CSM1.1(m)	HadGEM3
PC1 vs IOBM	0.98	0.95	0.98
PC2 vs IOD	0.87	0.70	0.89

4. Simulated teleconnections of Indian Ocean SST modes

4.1. *Relationship with ENSO*

ENSO is the strongest climatic variability on interannual time scales, and controls the TIO SSTA via an atmospheric bridge (Klein et al., 1999; Alexander et al., 2002). Figure 6 illustrates the lag correlation between the Niño3.4 and IOBM indices. The El Niño-induced surface flux change leads to a positive phase of the IOBM in boreal winter. The air–sea interaction over Indo-Pacific oceans sustain the IOBM warming to boreal summer (Du et al., 2009; Fig. 6a). This so-called "Indian Ocean capacitor effect" stores the ENSO forcing during the previous winter, and further affects the East Asian cli-

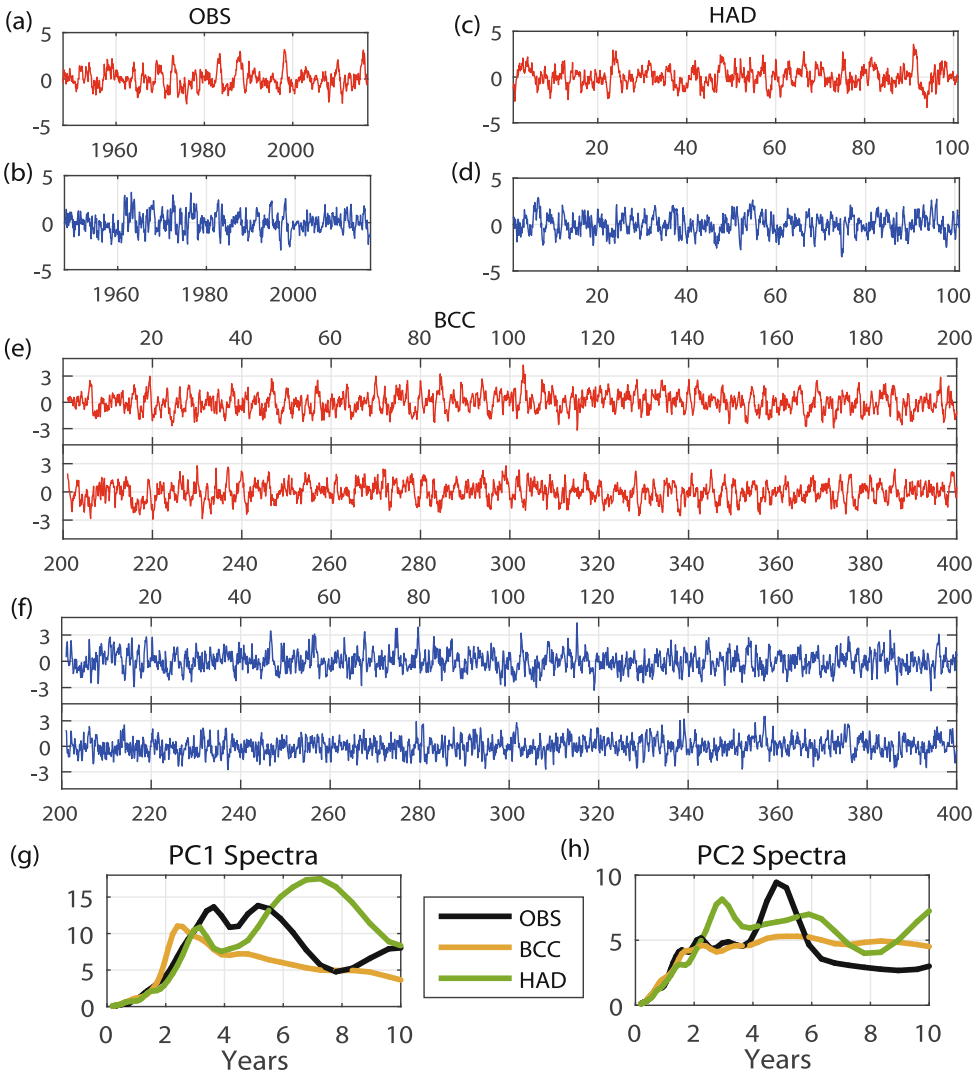

Fig. 5. Interannual variation of the first (red) and second (blue) EOF component in the (a, b) observation and the simulations by (c, d) HadGEM3 and (e, f) BCC_CSM1.1(m). (g, h) Spectra of (g) EOF PC1 and (h) EOF PC2 in the observations (black) and the simulations by BCC_CSM1.1(m) (yellow) and HadGEM3 (green).

mate in boreal summer (Xie et al., 2009). A previous study showed that this ENSO–IOBM relationship is simulated well by CMIP5 models (Du et al., 2013). As demonstrated in Figs. 6b and c, both BCC_CSM1.1(m) and HadGEM3 capture the TIO warming following El Niño. This simulated warming persists during boreal summer as observed, implying realistic Indo- Pacific air–sea interaction in both models.

The relationship between the IOD and ENSO is still a matter of debate. Some studies emphasize the dependence of the IOD on ENSO (e.g., Dommenget and Latif, 2002; Dommenget, 2011). As shown in Fig. 6, the IOD leads Niño3.4 by one season in the observation, with a significant lag correlation reaching 0.5 at the 99% confidence level (based on the Student's *t*-test). BCC_CSM1.1(m) is able to simulate this lag correlation, while the IOD–ENSO relationship is weak in HadGEM3. Given the fact that several IOD events have occurred without coinciding with ENSO, other studies have suggested the IOD as an inherent mode of internal variability within the TIO (Behera et al., 1999; Webster et al., 1999; Ashok et al., 2003; Yamagata et al., 2003). The WES and thermocline feedbacks have been suggested as fundamental to IOD growth (Li et al., 2003; Liu et al., 2011). A recent modeling study suggested that only one-third of the total IOD variance is forced by ENSO (Yang et al., 2015). Here, we find that 43% of all IOD events in the observation are accompanied by ENSO events. In the simulations by BCC_CSM1.1(m) and HadGEM3, 45% and 35% of all IOD events co-occur with ENSO events, respectively. Thus, the dependence of the IOD on ENSO is simulated well.

Recent studies have found that the IOD is not only a passive response to ENSO, but it can also affect ENSO properties. Coupled modeling experiments suggest that the ENSO amplitude is larger with than without IOD forcing (Yu et al., 2002). As shown in Fig. 7, El Niño events accompanied

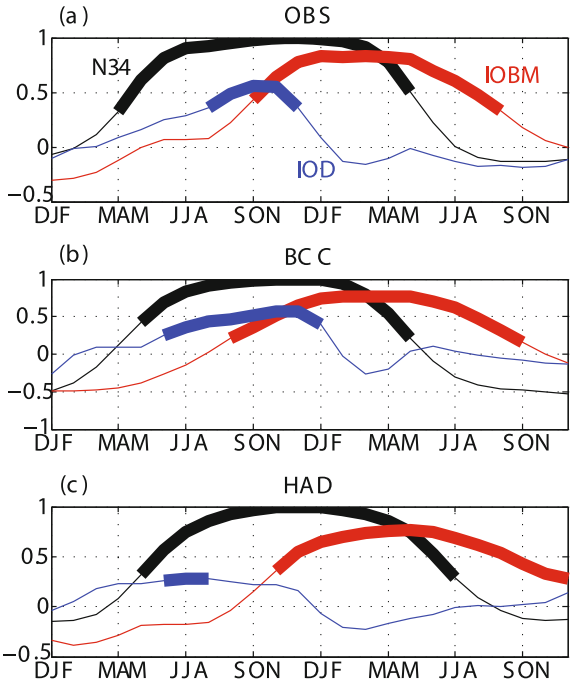

Fig. 6. Lag correlation of the November–January Niño3.4 anomaly with Niño3.4 (black), IOBM (red) and IOD (blue) anomalies in the (a) observation and the simulations by (b) BCC_CSM1.1(m) and (c) HadGEM3. Thick curves represent significant correlations at the >99% confidence level based on the Student's *t*-test.

by positive IOD events are generally stronger than pure El Niño, which is simulated well by BCC_CSM1.1(m) (Fig. 7b). However, La Niña events exhibit similar amplitudes with or without negative IOD forcing, which is successfully captured by HadGEM3 (Fig. 7f). Annamalai et al. (2005) pointed out that El Niño grows faster during boreal fall when coinciding with an IOD, as opposed to without (also see Fig. 7a), which is reproduced by BCC_CSM1.1(m). There is also evidence for a more rapid decay of El Niño when associated with an IOD event than without (Fig. 7a), due to the IOD-induced easterly wind over the tropical Pacific (Kug and Kang, 2006). As shown in Figs. 7b and c, this rapid decay of El Niño with a positive IOD is captured well by both BCC_CSM1.1(m) and HadGEM3. Given the remarkable impact of the IOD on ENSO, it is often used as a key factor in statistical ENSO prediction models (Ren et al., 2017).

4.2. *Local and remote impacts of the IOBM*

Figure 8 compares the geopotential height changes in the upper troposphere for different phases of the IOBM. The SAH is evident around the Tibetan Plateau during boreal summer. The variations and displacements of the SAH lead to rainfall anomalies over East Asia (Zhang et al., 2002). Huang et al. (2011) pointed out that IOBM warming results in a strengthening and southward extension of the SAH (also see Fig. 8a) via changing the equivalent potential temperature in the boundary layer. Although the model biases appear in the specific SAH value, a bigger (smaller) and stronger

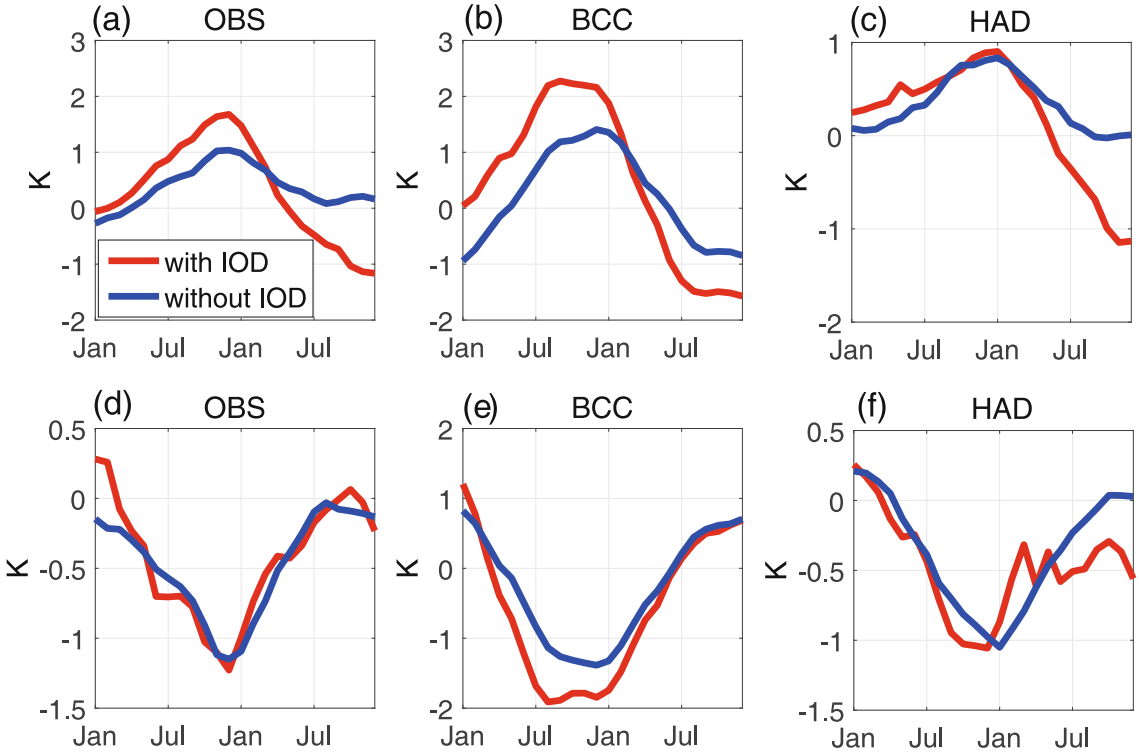

Fig. 7. Composites of the evolution of the Niño3.4 anomaly (units: °C) for the (a–c) El Niño and (d–f) La Niña years with (red) or without (blue) the coexistence of IOD years, from the (a, d) observations and the simulations by (b, e) BCC_CSM1.1(m) and (c, f) HadGEM3. The El Niño (La Niña) years are defined when the Niño3.4 anomaly reaches 0.5°C (−0.5°C). The IOBM (IOD) years are defined when the IOBM (IOD) index reaches one standard deviation.

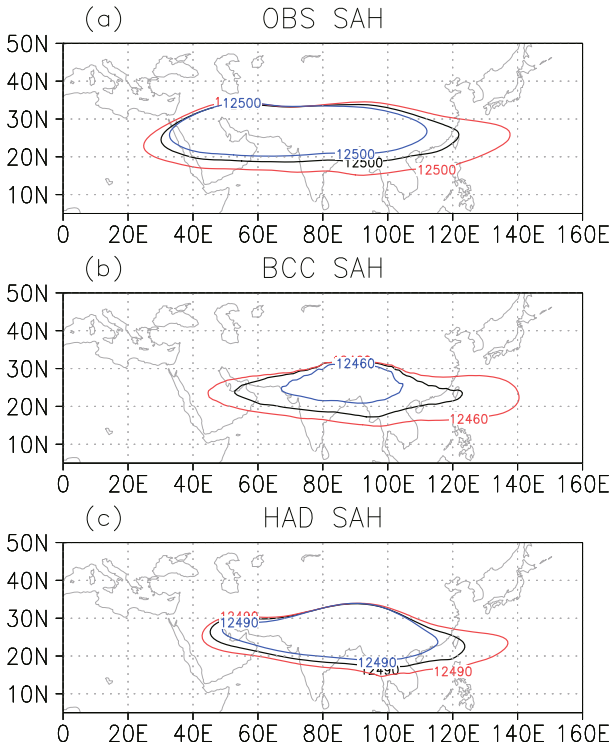

Fig. 8. Composites of the JJA SAH (units: gpm) in the climatology (black), warm IOBM years (red) and cold IOBM years (blue), from the (a) observations and the simulations by (b) BCC_CSM1.1(m) and (c) HadGEM3.

(weaker) SAH is reproduced when the TIO warms up (cools down) in both BCC_CSM1.1(m) and HadGEM3. This realistic IOBM–SAH relationship helps to give reasonable IOBM teleconnections over East Asia.

It is now well known that the IOBM acts as a capacitor that anchors the impact of ENSO in the previous winter (Xie et al., 2009). El Niño-induced TIO warming persists to boreal summer (Fig. 6) and excites a baroclinic Kelvin wave into the Pacific, which leads to the strengthening of the anomalous anticyclone over the northwestern Pacific (Fig. 9a). The resultant southwesterly wind anomaly brings water vapor from the ocean and enhances the rainfall over the Yangtze River valley (Fig. 9a). It is interesting that the cooling of the TIO induces the cyclonic wind anomalies over the northwestern Pacific, which is not as pronounced as that in the warming cases (Fig. 9b). This IOBM teleconnection is captured by half of the CMIP5 models (Du et al., 2013). As shown in Fig. 9, the atmospheric response to IOBM forcing is successfully simulated by HadGEM3, with realistic ACC changes over the northwestern Pacific and reasonable summer rainfall changes over the Yangtze River valley. In the simulations by BCC_CSM1.1(m), although the TIO warming (cooling) induces realistic easterly (westerly) wind anomalies over the TIO, the anomalous anticyclone (cyclone) over the northwestern Pacific is not as strong as in the observation (Figs. 9c and d). Consequently, the summer rainfall over the Yangtze River valley increases (decreases) following TIO warming (cooling); however, the changes are small compared with the observation. Since the northwestern Pacific subtropical high (NWPSH) is important for Yangtze River rainfall, it is very helpful to understand the causes of this weakened teleconnection between the IOBM and NWPSH in BCC_CSM1.1(m).

In a recent review paper, Xie et al. (2016) revealed that the air–sea coupling over the Indo-western Pacific Ocean plays an important role in the IOBM–NWPSH teleconnection. Following a Gill-type solution, the TIO warming can induce an easterly wind anomaly from the western Pacific to the northern TIO. On the one hand, this easterly wind anomaly further warms the TIO SST by reducing the local evaporation over the northern TIO, because the climatological wind is westerly due to a strong South Asian monsoon. On the other hand, this easterly wind anomaly increases the evaporation and cools the SST over the tropical northwestern Pacific due to the strong climatological trade wind. In turn, the warming over the TIO and cooling over the northwestern Pacific amplify the easterly wind anomaly, which then stimulates the strengthening of the NWPSH (Du et al., 2011). Thus, the IOBM-induced easterly wind anomaly is an indicator of the air–sea coupling over the Indo-western Pacific Ocean. Because of the asymmetric responses of the NWPSH to TIO warming and cooling phases, Fig. 10 focuses on the TIO warming cases. In the observation, the easterly wind anomaly over the Indo-western Pacific Ocean is significantly correlated (99% confidence level; Student's *t*-test) with the TIO SSTA. HadGEM3 basically captures this relationship, but it is not so robust in BCC_CSM1.1(m). This weak air–sea coupling over the Indo-western Pacific Ocean explains the underestimation of the NWPSH response to TIO warming in BCC_CSM1.1(m).

Next, the IOBM-induced circulation changes in the middle troposphere are investigated. Figure 11 demonstrates the configuration of the geopotential height at 500 hPa during warm and cold phases of the IOBM. In the observation, two dominant circulation patterns are evident during warm IOBM events. In the meridional direction over East Asia, the geopotential height anomalies show a high–low–high pattern from the tropics to the midlatitudes, which resembles the so-called "East Asia–Pacific" pattern (Huang and Sun, 1992). In the zonal direction, a stronger Urals blocking high (UL) and Okhotsk blocking high (OB) are observed when the TIO warms up. Previous studies have suggested that the "high–low–high EAP" pattern and strengthening of the UL and OB lead to the convergence of cold and warm air over Yangtze River valley (Zhang and Tao, 1998; Zhao et al., 2016). As a result, the configuration of the circulation induced by TIO warming is conducive to abundant rainfall over the valley. In the simulations by BCC_CSM1.1(m) and HadGEM3, the "high–low–high" tripole EAP pattern is not captured well. Instead, a "high–low" dipole pattern occurs under TIO warming. Thus, the strengthening of the OB is not simulated by both models. The stronger OB is simulated by HadGEM3, but the amplitude is largely underestimated. In BCC_CSM1.1(m), the OB remains unchanged. For the negative phases of the IOBM, the observed configuration of the

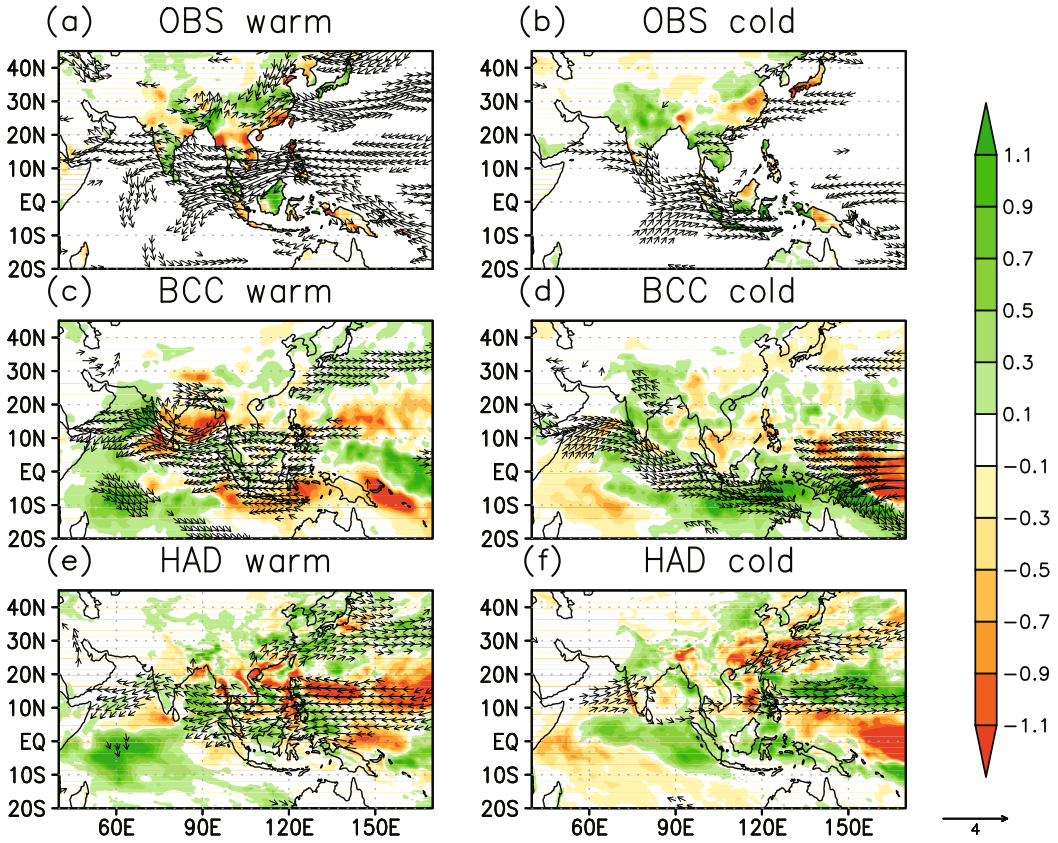

Fig. 9. Composites of JJA rainfall (units: mm month^{-1}) and horizontal wind at 850 hPa (units: m s^{-1}) during (a, c, e) warm IOBM years and (b, d, f) cold IOBM years, from the (a, b) observations (land only) and the simulations by (c, d) BCC_CSM1.1(m) and (e, f) HadGEM3.

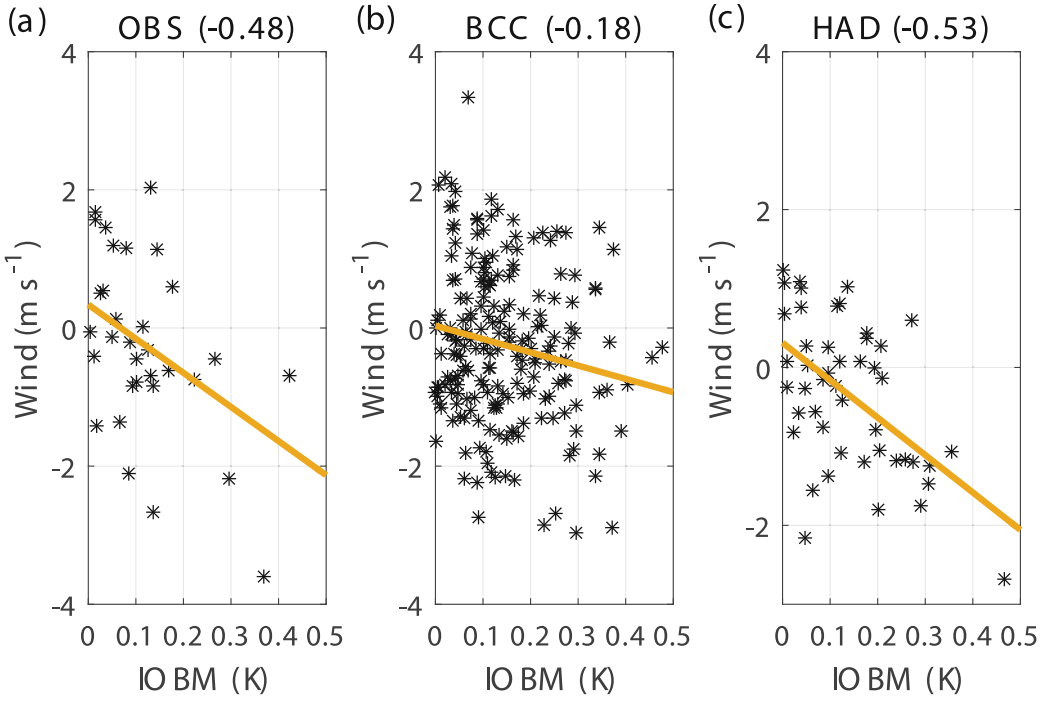

Fig. 10. Scatterplot of the zonal wind anomaly at 850 hPa averaged over the Indo-western Pacific Ocean (5°–15°N, 80°–130°E) against the IOBM indices in the (a) observation and the simulations by (b) BCC_CSM1.1(m) and (c) HadGEM3. The straight lines indicate the linear trend. The correlation coefficients are given in parentheses. It should be noted that only the warm phases of the IOBM are shown here, due to the asymmetric responses of the East Asian climate to the cold and warm TIO forcing.

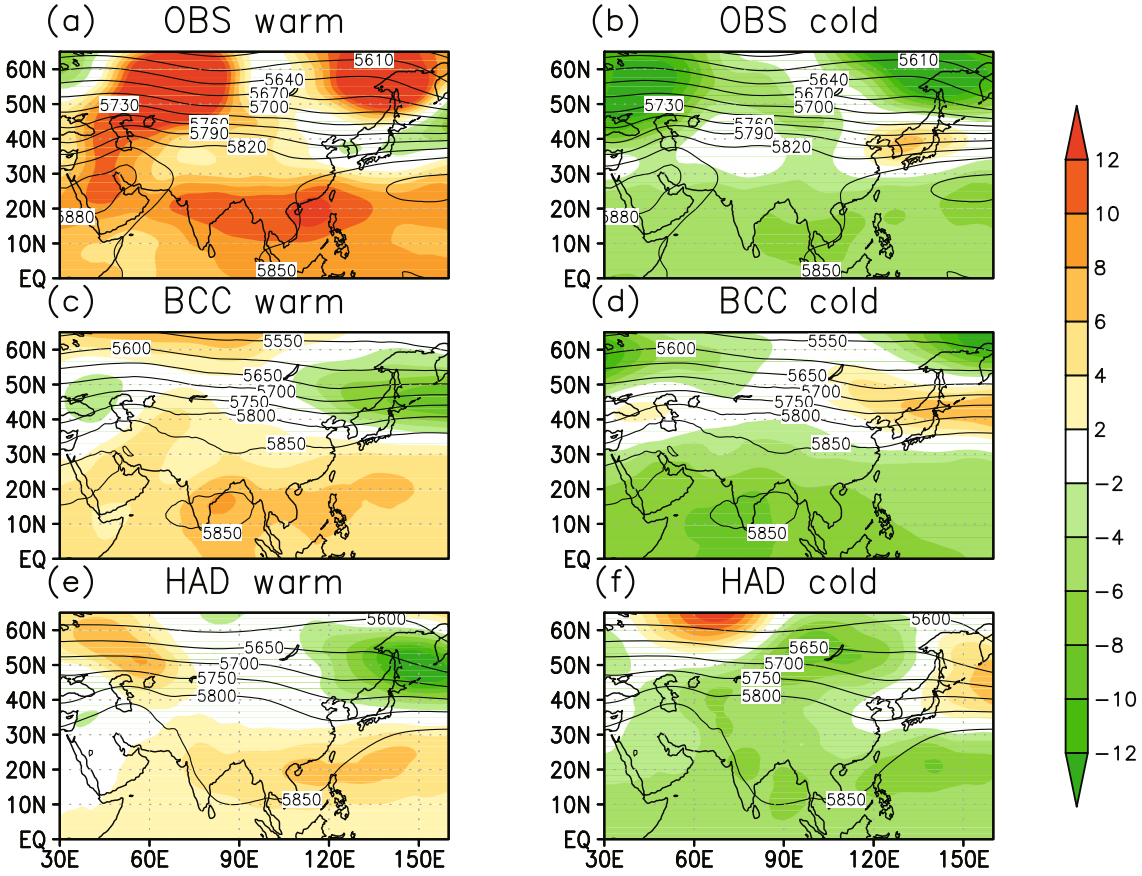

Fig. 11. Composites of JJA climatological (contours) and anomalous (shading) geopotential height at 500 hPa during (a, c, e) warm IOBM years and (b, d, f) cold IOBM years, from the (a, b) observations and the simulations by (c, d) BCC_CSM1.1(m) and (e, f) HadGEM3.

circulation at 500 hPa is simulated well by BCC_CSM1.1(m).

The realistic simulations of the IOBM and its teleconnections enable skillful seasonal predictions of the East Asian climate during boreal summer by the seasonal prediction systems of BCC_CSM1.1(m) and GloSea5 (the operational system at the UK Met Office using HadGEM3). As illustrated by Table 2, when initialized in May, the correlation skill of the IOBM is as high as 0.9 for both models. The variation of the NWPSH is predicted well by GloSea5, with the correlation skill reaching 0.9. Due to the weak biases of the IOBM-induced ACC over the northwestern Pacific, the prediction skill of the NWPSH is slightly lower than that of GloSea5. However, the correlation skill still reaches 0.7, which is significant at the 99% confidence level using the Student's *t*-test. The successful prediction of the NWPSH offers realistic water vapor transport. Thus, GloSea5 and BCC_CSM1.1(m) are capable of predicting the variation in summer rainfall over Yangtze River valley (Li et al., 2016), with the correlation skill reaching 0.54 and 0.47, respectively.

4.3. *Local and remote impacts of the IOD*

Previous studies have shown important climatic impacts of the IOD (Saji and Yamagata, 2003), including the severe East African flood during the two strongest positive IOD years in 1994 (Behera et al., 1999) and 1997 (Birkett et al., 1999; Webster et al., 1999), and the drought in 2016 (Lu et al., 2017). Figure 12 illustrates the rainfall and wind anomalies during boreal fall during IOD events. The impact from ENSO has first been removed by linear regression. It is clear that a positive (negative) IOD induces easterly (westerly) wind anomalies over the equatorial Indian Ocean, which brings above-normal (below-normal) rainfall over East Africa during boreal fall. The influence of the IOD on East African rainfall has been reproduced in some model simulations (Latif et al., 1999; Ummenhofer et al., 2009). Here, it is demonstrated that this IOD–East Africa rainfall relationship is reproduced well by BCC_CSM1.1(m) and HadGEM3 (Fig. 12). As a result, real-time predictions based on these

Table 2. Correlation skill of the IOBM, SLP over the northwestern Pacific (10°–20°N, 130°–155°E), and the Yangtze River rainfall (25°–35°N, 91°–122°E) during boreal summer from the BCC_CSM1.1(m) and GloSea5 seasonal forecasts when initialized in May.

	IOBM	SLP over northwestern Pacific	Precipitation over the Yangtze River
BCC_CSM1.1(m)	0.86	0.73	0.47
GloSea5	0.90	0.89	0.54

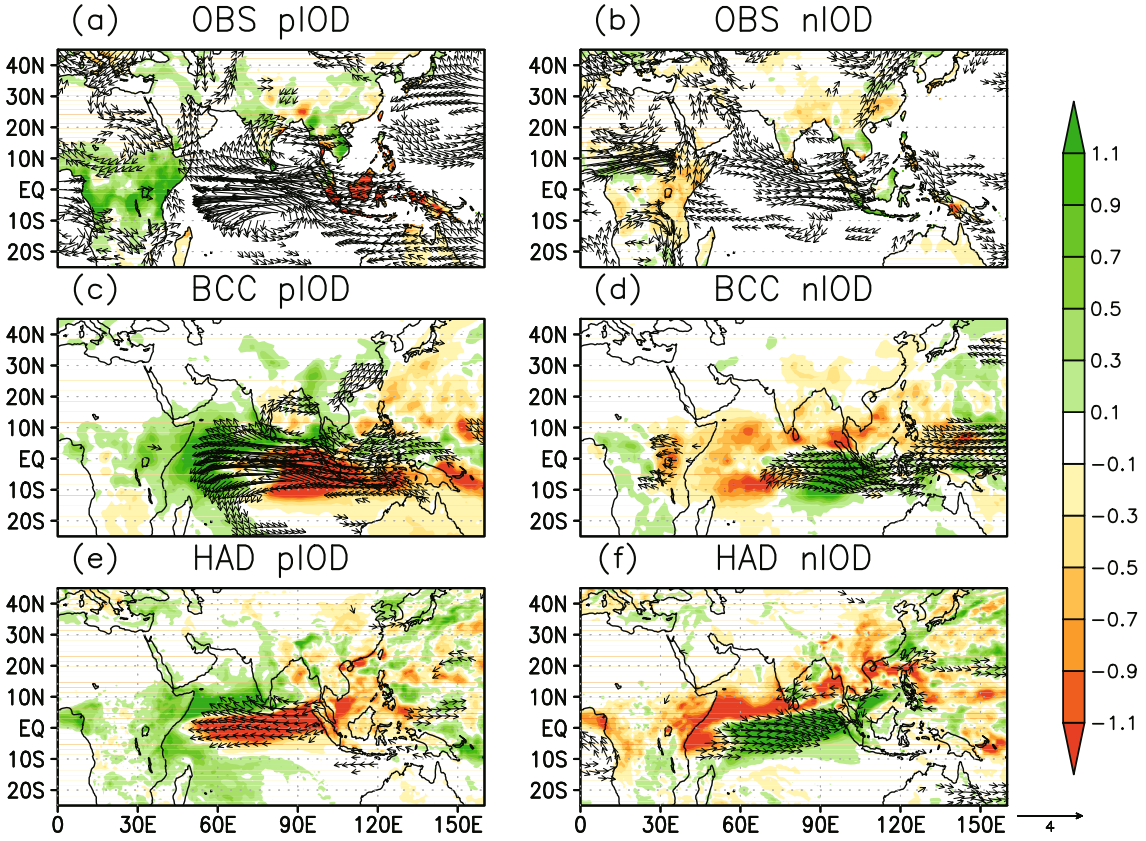

Fig. 12. Composites of SON rainfall (units: mm month^{-1}) and horizontal wind at 850 hPa (units: m s^{-1}) during (a, c, e) positive IOD years and (b, d, f) negative IOD years, in the (a, b) observation (precipitation over land only) and the simulations by (c, d) BCC_CSM1.1(m) and (e, f) HadGEM3. The influence of ENSO has first been removed by linear regression.

two models captured the 2016 East African drought two seasons ahead (Lu et al., 2017).

During positive IOD events, the cooling in the eastern TIO induces equatorial easterly wind and excites cyclonic wind anomalies over the Bay of Bengal (BOB) following a Gill-type response (Gill, 1980). As a result, the northern BOB is controlled by westerly wind anomalies (Fig. 12a), which intensify the India–Burma trough and increase the rainfall over the eastern Indochina Peninsula and southwestern China (Qiu et al., 2014; Lu and Ren, 2016b). As shown in Fig. 13, the observed southwestern China rainfall during boreal fall is significantly correlated with the IOD index. However, this relationship is not simulated by either BCC_CSM1.1(m) or HadGEM3 (Figs. 13b and c). Consequently, the southwestern China rainfall during boreal fall is not predicted well by the seasonal prediction systems using these two models. The prediction skill is as low as 0.35 in the hindcast by BCC_CSM1.1(m), which is insignificant even at the 90% confidence level.

5. Summary and discussion

The SST variations in the TIO not only affect the local climate around the Indian Ocean region, but also induce global impacts, including East Asia. Given the important role of the TIO SSTA in modulating the climate anomalies, it is necessary to assess how well the major TIO SST modes, as well as their teleconnections, are simulated by our operational models. In this study, the control experiments of BCC_CSM1.1(m) and HadGEM3 are evaluated.

It is demonstrated that the climatological monsoonal wind and SST patterns are generally simulated well by BCC_CSM1.1(m) and HadGEM3. The leading two modes at interannual time scales, the IOBM and IOD, are also reproduced well by both models. Similar to the observations and most CMIP5 models (Du et al., 2013), the simulated first EOF mode shows a basin-wide pattern, while the simulated second mode exhibits a zonal dipole pattern. The explained variances of the simulated first EOFs are smaller than in the observations, which is a common bias for many CMIP5 models (Du et al., 2013). The explained variances of the simulated second EOFs are comparable to the observations. The seasonal cycles of the IOBM and IOD variability are captured well by both models, except that BCC_CSM1.1(m) overestimates the IOD variability in boreal winter and early spring. Following the periodicity biases in ENSO simulations (Lu and Ren, 2016a), the periodicity of the IOBM is also too short compared with the observation. The spectrum of IOD variability is not captured by either model.

The SST variation in the TIO is tightly connected to

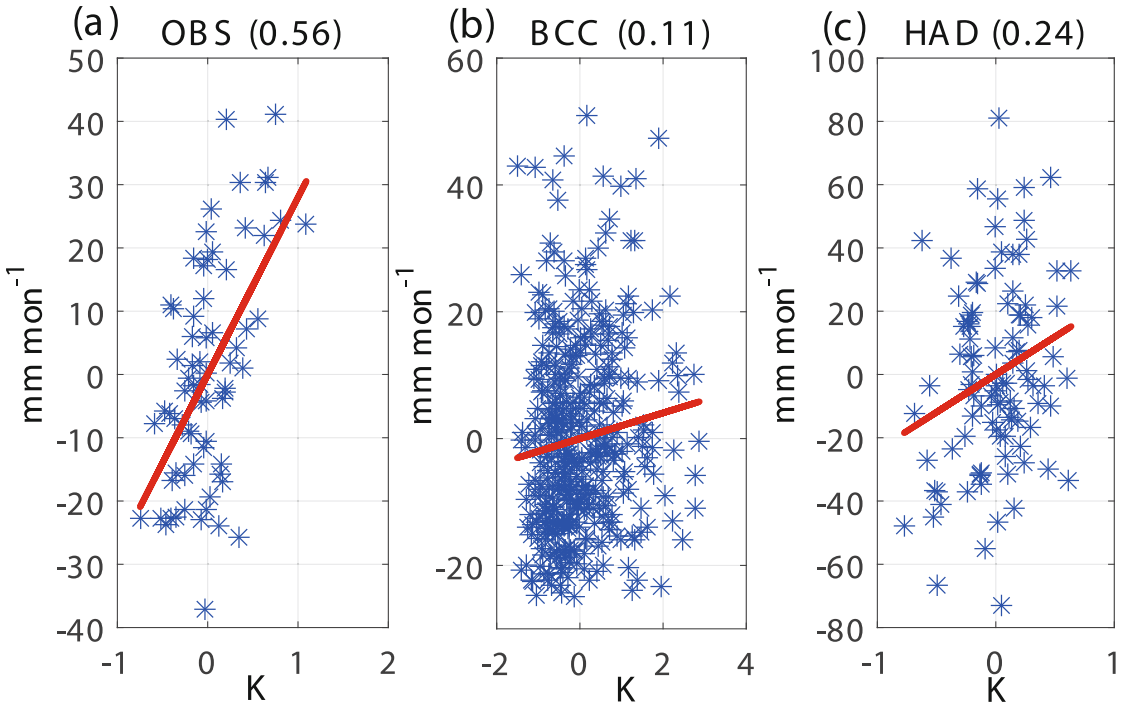

Fig. 13. Scatterplots of the precipitation over southwestern China (24°–28°N, 103°–109°E) against the IOD indices in the (a) observation and the simulations by (b) BCC_CSM1.1(m) and (c) HadGEM3. The linear fitting line is indicated.

ENSO. Like most CMIP5 models (Du et al., 2013), the persistent IOBM warming following El Niño is successfully simulated by both models. The dependence of the IOD on ENSO is reproduced by BCC_CSM1.1(m), implying the presence of realistic IOD dynamics. IOD events in HadGEM3 are more independent of ENSO forcing, indicating strong air–sea interaction within the Indian Ocean basin (Johnson et al., 2017). The IOD can also feed back to ENSO. The faster decay of El Niño with the coexistence of the IOD (Kug and Kang, 2006) is reproduced by both models. BCC_CSM1.1(m) also captures the relationship of a stronger El Niño when coinciding with an IOD event rather than without (Yu et al., 2002). The realistic TIO SST–ENSO relationships indicate the successful representation of TIO–Pacific feedbacks in BCC_CSM1.1(m) and HadGEM3.

Observational evidence shows that IOBM warming can affect local impacts, such as a strengthening of the SAH, which is simulated well by both models. The IOBM warming induces easterly wind anomalies over the TIO and northwestern Pacific, which intensifies the NWPSH and increases the summer rainfall over the Yangtze River valley (Xie et al., 2009). Like half of the CMIP5 models (Du et al., 2013), this so-called "Indian Ocean capacitor" effect is simulated well by HadGEM3. As a result, the Met Office seasonal prediction system (GloSea5) based on this model shows high skill in predicting the NWPSH and Yangtze River summer rainfall. In BCC_CSM1.1(m), the response of the NWPSH to IOBM forcing is weaker than observed, and thus the prediction skill of Yangtze River summer rainfall is slightly lower than that in GloSea5. For the impact of the IOD, both models successfully capture the response of East African rainfall to IOD forcings. However, the control by the IOD of the precipitation over southwestern China during boreal fall is not clear in either model. Consequently, the prediction skill of precipitation over southwestern China during boreal fall is relatively low. Our results suggest that realistic simulations of the TIO SSTA and its impact are the foundation of skillful seasonal predictions.

Acknowledgements. This work is jointly supported by the National Key Research and Development Program of China (Grant No. 2016YFA0602104), the China Meteorological Special Program (Grant No. GYHY201506013), and the National Science Foundation (Grant No. 41605116). This work and its contributors (Bo LU, Hong-Li REN, Rosie EADE, and Martin ANDREWS) were supported by the UK–China Research & Innovation Partnership Fund through the Met Office Climate Science for Service Partnership (CSSP) China as part of the Newton Fund.

REFERENCES

Alexander, M. A., I. Bladé, M. Newman, J. R. Lanzante, N. C. Lau, and J. D. Scott, 2002: The atmospheric bridge: The influence of ENSO teleconnections on air-sea interaction over the global oceans. *J. Climate*, **15**, 2205–2231, https://doi.org/10.1175/1520-0442(2002)015<2205:TABTIO>2.0.CO;2.

Allan, R., and Coauthors, 2001: Is there an Indian Ocean dipole, and is it independent of the El Niño-Southern Oscillation? *CLIVAR Exchanges*, **6**, 18–22.

Annamalai, H., S.-P. Xie, J.-P. McCreary, and R. Murtugudde, 2005: Impact of Indian Ocean sea surface temperature on de-

veloping El Niño. *J. Climate*, **18**, 302–319, https://doi.org/10.1175/JCLI-3268.1.

Ashok, K., Z. Y. Guan, and T. Yamagata, 2003: Influence of the Indian Ocean Dipole on the Australian winter rainfall. *Geophys. Res. Lett*., **30**(15), 1821, https://doi.org/10.1029/2003GL017926.

Baquero-Bernal, A., M. Latif, and S. Legutke, 2002: On dipole-like variability of sea surface temperature in the tropical Indian Ocean. *J. Climate*, **15**(11), 1358–1368, https://doi.org/10.1175/1520-0442(2002)015<1358:ODVOSS>2.0.CO;2.

Behera, S. K., R. Krishnan, and T. Yamagata, 1999: Unusual ocean-atmosphere conditions in the tropical Indian Ocean during 1994. *Geophys. Res. Lett*., **26**, 3001–3004, https://doi.org/10.1029/1999GL010434.

Birkett, C., R. Murtugudde, and R. Allan, 1999: Indian Ocean climate event brings floods to East Africa's lakes and the Sudd Marsh. *Geophys. Res. Lett*., **26**, 1031–1034, https://doi.org/10.1029/1999GL900165.

Black, E, J. Slingo, and K. R. Sperber, 2003: An observational study of the relationship between excessively strong short rains in coastal East Africa and Indian Ocean SST. *Mon. Wea. Rev*., **131**, 74–94, https://doi.org/10.1175/1520-0493(2003)131<0074:AOSOTR>2.0.CO;2.

Chan, S. C., S. K. Behera, and T. Yamagata, 2008: Indian Ocean Dipole influence on South American rainfall. *Geophys. Res. Lett*., **35**, L14S12, https://doi.org/10.1029/2008GL034204.

Chiang, J. C. H., and A. H. Sobel, 2002: Tropical tropospheric temperature variations caused by ENSO and their influence on the remote tropical climate. *J. Climate*, **15**, 2616–2631, https://doi.org/10.1175/1520-0442(2002)015<2616:TTTVCB>2.0.CO;2.

Dommenget, D., and M. Jansen, 2009: Predictions of Indian Ocean SST indices with a simple statistical model: A null hypothesis. *J. Climate*, **22**(18), 4930–4938, https://doi.org/10.1175/2009JCLI2846.1.

Dommenget, D., and M. Latif, 2002: A cautionary note on the interpretation of EOFs. *J. Climate* **15**(2), 216–225, https://doi.org/10.1175/1520-0442(2002)015<0216:ACNOTI>2.0.CO;2.

Dommenget, D., 2011: An objective analysis of the observed spatial structure of the Tropical Indian Ocean SST variability. *Climate Dyn*., **36**, 2129–2145, https://doi.org/10.1007/s00382-010-0787-1.

Du, Y., and S.-P. Xie, 2008: Role of atmospheric adjustments in the tropical Indian Ocean warming during the 20th century in climate models. *Geophys. Res. Lett*., **35**, L08712, https://doi.org/10.1029/2008GL033631.

Du, Y., S.-P. Xie, G. Huang, and K. M. Hu, 2009: Role of air–sea interaction in the long persistence of El Niño–induced North Indian Ocean warming. *J. Climate*, **22**, 2023–2038, https://doi.org/10.1175/2008JCLI2590.1.

Du, Y., L. Yang, and S.-P. Xie, 2011: Tropical Indian Ocean influence on Northwest Pacific tropical cyclones in summer following strong El Niño. *J. Climate*, **24**, 315–322, https://doi.org/10.1175/2010JCLI3890.1.

Du, Y., S.-P. Xie, Y. L. Yang, X. T. Zheng, L. Liu, and G. Huang, 2013: Indian Ocean variability in the CMIP5 multimodel ensemble: The Basin mode. *J. Climate*, **26**, 7240–7266, https://doi.org/10.1175/JCLI-D-12-00678.1.

Gill, A. E., 1980: Some simple solutions for heat-induced tropical circulation. *Quart. J. Roy. Meteor. Soc*., **106**, 447–462, https://doi.org/10.1002/qj.49710644905.

Harris, I., P. D. Jones, T. J. Osborn, and D. H. Lister, 2014: Updated high-resolution grids of monthly climatic observations—The CRU TS3.10 Dataset. *Int. J. Climatol*., **34**, 623–642, https://doi.org/10.1002/joc.3711.

Huang, G., X. Qu, and K. M. Hu, 2011: The impact of the tropical Indian Ocean on South Asian high in boreal summer. *Adv. Atmos. Sci*., **28**, 421–432, https://doi.org/10.1007/s00376-010-9224-y.

Huang, R. H., and F. Y. Sun, 1992: Impacts of the tropical western Pacific on the East Asian summer monsoon. *J. Meteor. Soc. Japan*, **70**, 243–256, https://doi.org/10.2151/jmsj1965.70.1B_243.

Johnson, S. J., A. Turner, S. Woolnough, G. Martin, and C. MacLachlan, 2017: An assessment of Indian monsoon seasonal forecasts and mechanisms underlying monsoon interannual variability in the Met Office GloSea5-GC2 system. *Climate Dyn*., **48**(5), 1447–1465, https://doi.org/10.1007/s00382-016-3151-2.

Kalnay, E., and Coauthors, 1996: The NCEP/NCAR 40-year reanalysis project. *Bull. Amer. Meteor. Soc*., **77**, 437–472, https://doi.org/10.1175/1520-0477(1996)077<0437:TNYRP>2.0.CO;2.

Klein, S. A., B. J. Soden, and N. C. Lau, 1999: Remote Sea surface temperature variations during ENSO: Evidence for a tropical atmospheric bridge. *J. Climate*, **12**, 917–932, https://doi.org/10.1175/1520-0442(1999)012<0917:RSSTVD>2.0.CO;2.

Kug, J.-S., and I.-S. Kang, 2006: Interactive feedback between ENSO and the Indian Ocean. *J. Climate*, **19**, 1784–1801, https://doi.org/10.1175/JCLI3660.1.

Latif, M., D. Dommenget, M. Dima, and A. Grötzner, 1999: The role of Indian Ocean sea surface temperature in forcing East African rainfall anomalies during December–January 1997/98. *J. Climate*, **12**(12), 3497–3504, https://doi.org/10.1175/1520-0442(1999)012<3497:TROIOS>2.0.CO;2.

Li, C. F., and Coauthors, 2016: Skillful seasonal prediction of Yangtze river valley summer rainfall. *Environmental Research Letters*, **11**, 094002, https://doi.org/10.1088/1748-9326/11/9/094002.

Li, G., S.-P. Xie, and Y. Du, 2015: Monsoon-induced biases of climate models over the tropical Indian Ocean. *J. Climate*, **28**, 3058–3072, https://doi.org/10.1175/JCLI-D-14-00740.1.

Li, T., B. Wang, C. P. Chang, and Y. S. Zhang, 2003: A theory for the Indian Ocean dipole–zonal mode. *J. Atmos. Sci*., **60**, 2119–2135, https://doi.org/10.1175/1520-0469(2003)060<2119:ATFTIO>2.0.CO;2.

Liu, L., W. D. Yu, and T. Li, 2011: Dynamic and thermodynamic air–sea coupling associated with the Indian Ocean dipole diagnosed from 23 WCRP CMIP3 models. *J. Climate*, **24**, 4941–4958, https://doi.org/10.1175/2011JCLI4041.1.

Liu, Z. Y., and M. Alexander, 2007: Atmospheric bridge, oceanic tunnel, and global climatic teleconnections. *Rev. Geophys*., **45**, RG2005, https://doi.org/10.1029/2005RG000172.

Lu, B., and H.-L. Ren, 2016a: Improving ENSO periodicity simulation by adjusting cumulus entrainment in BCC_CSMs. *Dyn. Atmos. Oceans*, **76**, 127–140, https://doi.org/10.1016/j.dynatmoce.2016.10.005.

Lu, B., and H.-L. Ren, 2016b: SST-forced interdecadal deepening of the winter India–Burma trough since the 1950s. *J. Geophys. Res*., **121**(6), 2719–2731, https://doi.org/10.1002/2015JD024393.

Lu, B., and Coauthors, 2017: An extreme negative Indian Ocean Dipole event in 2016: Dynamics and predictability. *Climate*

Dyn., https://doi.org/10.1007/s00382-017-3908-2. (in Press)

MacLachlan, C., and Coauthors, 2015: Global Seasonal forecast system version 5 (GloSea5): A high-resolution seasonal forecast system. *Quart. J. Roy. Meteor. Soc*., **141**(689), 1072–1084, https://doi.org/10.1002/qj.2396.

Qiu, Y., W. J. Cai, X. G. Guo, and B. Ng, 2014: The asymmetric influence of the positive and negative IOD events on China's rainfall. *Scientific Reports*, **4**, 4943, https://doi.org/10.1038/srep04943.

Rayner, N. A., P. Brohan, D. E. Parker, C. K. Folland, J. J. Kennedy, M. Vanicek, T. J. Ansell, and S. F. B. Tett, 2006: Improved analyses of changes and uncertainties in sea surface temperature measured in situ since the mid-nineteenth century: The HadSST2 dataset. *J. Climate*, **19**, 446–469, https://doi.org/10.1175/JCLI3637.1.

Ren, H. L., and Coauthors, 2017: Prediction of primary climate variability modes at the Beijing Climate Center. *J. Meteor. Res*., **31**, 204–223, https://doi.org/10.1007/s13351-017-6097-3.

Saji, N. H., and T. Yamagata, 2003: Possible impacts of Indian Ocean Dipole mode events on global climate. *Climate Res*., **25**, 151–169, https://doi.org/10.3354/cr025151.

Saji, N. H., B. N. Goswami, P. N. Vinayachandran, and T. Yamagata, 1999: A dipole mode in the tropical Indian Ocean. *Nature*, **401**, 360–363, https://doi.org/10.1038/43854.

Schott, F. A., S.-P. Xie, and J. P. McCreary Jr., 2009: Indian Ocean circulation and climate variability. *Rev. Geophys*., **47**, RG1002, https://doi.org/10.1029/2007RG000245.

Stevenson, S., B. Fox-Kemper, M. Jochum, B. Rajagopalan, and S. G. Yeager, 2010: ENSO model validation using wavelet probability analysis. *J. Climate*, **23**(20), 5540–5547, https://doi.org/10.1175/2010JCLI3609.1.

Ummenhofer, C. C., A. S. Gupta, M. H. England, and C. J. C. Reason, 2009: Contributions of Indian Ocean sea surface temperatures to enhanced East African rainfall. *J. Climate*, **22**, 993–1013, https://doi.org/10.1175/2008JCLI2493.1.

Wallace, J. M., E. M. Rasmusson, T. P. Mitchell, V. E. Kousky, E. S. Sarachik, and H. von Storch, 1998: On the structure and evolution of ENSO-related climate variability in the tropical Pacific: Lessons from TOGA. *J. Geophys. Res*., **103**, 14241–14259, https://doi.org/10.1029/97JC02905.

Webster, P. J., A. M. Moore, J. P. Loschnigg, and R. R. Leben, 1999: Coupled ocean–atmosphere dynamics in the Indian Ocean during 1997-98. *Nature*, **401**, 356–360, https://doi.org/10.1038/43848.

Wittenberg, A. T., 2009: Are historical records sufficient to constrain ENSO simulations? *Geophys. Res. Lett*., **36**, L12702, https://doi.org/10.1029/2009GL038710.

Wu, T. W., and Coauthors, 2010: The Beijing Climate Center atmospheric general circulation model: Description and its performance for the present-day climate. *Climate Dyn*., **34**, 123–147, https://doi.org/10.1007/s00382-008-0487-2.

Xie, S.-P., K. M. Hu, J. Hafner, H. Tokinaga, Y. Du, G. Huang, and T. Sampe, 2009: Indian Ocean capacitor effect on Indo-western Pacific climate during the summer following El Niño. *J. Climate*, **22**, 730–747, https://doi.org/10.1175/2008JCLI2544.1.

Xie, S.-P., Y. Kosaka, Y. Du, K. M. Hu, J. S. Chowdary, and G. Huang, 2016: Indo-western Pacific ocean capacitor and coherent climate anomalies in post-ENSO summer: A review. *Adv. Atmos. Sci*., **33**(4), 411–432, https://doi.org/10.1007/s00376-015-5192-6.

Yamagata, T., S. K. Behera, S. A. Rao, and H. N. Sall, 2003: Comments on "Dipoles, temperature gradients, and tropical climate anomalies". *Bull. Amer. Meteor. Soc*., **84**, 1418–1422, https://doi.org/10.1175/BAMS-84-10-1418.

Yang, J. L., and Q. Y. Liu, 2008: The "charge/discharge" roles of the basin-wide mode of the Indian Ocean SST anomaly——influence on the South Asian High in summer. *Acta Oceanologica Sinica*, **30**, 12–19, https://doi.org/10.3321/j.issn:0253-4193.2008.02.002. (in Chinese with English abstract)

Yang, J. L., Q. Y. Liu, S. P. Xie, Z. Y. Liu, and L. X. Wu, 2007: Impact of the Indian Ocean SST basin mode on the Asian summer monsoon. *Geophys. Res. Lett*., **34**, L02708, https://doi.org/10.1029/2006GL028571.

Yang, Y., S.-P. Xie, L. X. Wu, Y. Kosaka, N. C. Lau, and G. A. Vecchi, 2015: Seasonality and predictability of the Indian Ocean Dipole mode: ENSO forcing and internal variability. *J. Climate*, **28**(20), 8021–8036, https://doi.org/10.1175/JCLI-D-15-0078.1.

Yu, J.-Y., C. R. Mechoso, J. C. McWilliams, and A. Arakawa, 2002: Impacts of the Indian Ocean on the ENSO cycle. *Geophys. Res. Lett*., **29**(8), 46-1–46-4, https://doi.org/10.1029/2001GL014098.

Yuan, Y., H. Yang, W. Zhou, and C. Y. Li, 2008: Influences of the Indian Ocean Dipole on the Asian summer monsoon in the following year. *Int. J. Climatol*., **28**, 1849–1859, https://doi.org/10.1002/joc.1678.

Zhang, Q., G. X. Wu, and Y. F. Qian, 2002: The bimodality of the 100 hPa South Asia high and its relationship to the climate anomaly over East Asia in summer. *J. Meteor. Soc. Japan*, **80**, 733–744, https://doi.org/10.2151/jmsj.80.733.

Zhang, Q. Y., and S. Y. Tao, 1998: Influence of Asian mid-high latitude circulation on East Asian summer rainfall. *Acta Meteorologica Sinica*, **56**, 199–211, https://doi.org/10.11676/qxxb1998.019. (in Chinese with English abstract)

Zhao, J. H., L. Yang, Y. X. Zeng, and G. L. Feng, 2016: Analysis of atmospheric circulation and prediction signals for summer rainfall patterns in southern China. *Chinese Journal of Atmospheric Sciences*, **40**(6), 1182–1198, https://doi.org/10.3878/j.issn.1006-9895.1601.15249. (in Chinese with English abstract)